Modeling the influence of the geometrical unsharpness on the neutron radiography and tomography images of porous materials

I.Yu. Zel [1],
[1] *Joint Institute for Nuclear Research,*
141980, Russia, Dubna, Joliot-Curie St. 6

Abstract

Beam divergence is one of the instrument resolution parameters in neutron computed tomography. In pinhole geometry, due to the finite size of the source, geometric unsharpness affects the transmission images and therefore influences the reconstructed data. In this paper, we propose an approach for deterministic simulation of this effect for a voxelized 3D object. The idea behind the proposed approach is to use multiple point sources at a pinhole position and collect transmission images from each of them. The implementation was done using the ASTRA toolbox by calculating cone beam projections from each point source. This approach was applied to a porous phantom. Artifacts associated with beam divergence were identified in the reconstructed data. The influence of beam divergence on the segmentation of pores by binarization of the reconstructed data has been considered.

Keywords: geometrical unsharpness, neutron tomography, ASTRA toolbox, porous material.

Citation: Zel IY. Modeling the influence of the geometrical unsharpness on the neutron radiography and tomography images of porous materials. Computer Optics 2025; 49(2): 327-333. DOI: 10.18287/2412-6179-CO-1478.

Acknowledgements: This work was supported by Russian Science Foundation, grant № 23-72-01031, https://rscf.ru/project/23-72-01031/.

Introduction

Computed tomography (CT) using neutron beams is a well-developed non-destructive imaging technique that not only complements traditional X-ray CT (XCT), but also has advantages in a number of applications [1 – 4]. The basic principles of neutron computed tomography (NCT) are the same as for XCT, although the experimental setup is less variable. Measurements are carried out in pinhole geometry with a scintillation screen and a CCD camera [5]. Essentially, NCT differs from XCT only by the difference in the type of interaction of neutrons with matter. The main parameters of pinhole geometry are the diameter of the pinhole (source) D and the distance from the source to the detector L. Thanks to $L >> D$, parallel beam geometry is a suitable approximation for ray tracing in NCT. The L/D ratio is related to the degree of beam divergence, or geometric blur, and is therefore used as one of the instrument resolution parameters [6]. In addition to geometric limitations, the resolution of the instrument is also affected by scintillator blur [7 – 9]. The latter can be measured in a radiography experiment through the edge-spread function (ESF) and the corresponding point-spread function (PSF) [10] determined. [7] shows the feasibility of deblurring radiographic images using measured PSF. However, it is still questionable whether the beam divergence effect can be represented by PSF and whether the PSF-based image deblurring procedure correctly restores the ideal transmission image produced by the parallel beam.

Among all image formation specifics in NCT, the influence of beam divergence on the tomography data is less studied. While Monte-Carlo-based simulations were reported for evaluating scintillator blur [11] and secondary scattering [12 – 13], no beam divergence simulation in NCT was reported to the best of our knowledge. The simulation of NCT will help not only in better understanding experimental data but may also be used for creating realistic data sets for machine learning applications in reconstruction, denoising, and segmentation.

In this work, we are focused on studying the influence of beam divergence on the NCT, specifically on radiography and reconstructed tomography data. We present the approach for deterministic simulation of NCT with rather flexible parametrization of the geometry of the experiment. A solid phantom containing pores of different diameters was chosen as the measurement object in our simulation of NCT for several reasons: porous materials are frequently tested by this method [14 – 16]; the pore-solid boundary is always clearly visible (large contrast in the reconstructed images); size of pores influences on how robust their boundary may be resolved due to any blurring effects, i.e., we also address to the segmentation problem (e.g., [17]).

1. Geometry and calculation approach

Image formation in a neutron tomography experiment depends largely on the neutron source, the size and shape of which are determined by the aperture used. If the aperture size is small enough, then a cone beam geometry can be considered for a given point source. However, in practice, due to low neutron flux, the aperture is left 1 – 10 cm in size, providing exposure times of a few seconds while maintaining low noise levels. Therefore, the real source of neutrons can be modeled by a set of point sources, each of which produces the cone beam transmission of the object. In our simulation of the neutron tomography experiment, the neutron source is defined as a discrete set of point sources lying in a plane (Fig. 1). The shape of the source, as well as the number of point sources, can be chosen arbitrarily; for example, in the case of a circle pinhole with radius r, the discrete coordinates of the point sources (x, y) are those satisfying $x^2+y^2\le r^2$. A cone beam transmission is obtained from each point source, and the sum of these images normalized by the incident intensity (open beam image) is thus the measured transmission of the object.

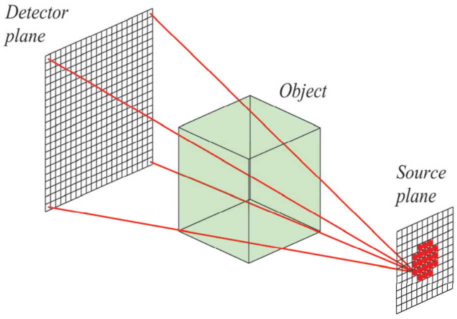

Fig. 1. Geometry of the simulation

The realization of such geometry was performed using the flexible ASTRA toolbox [18-20], in which the point source positions and the locations of the detector pixels are defined in a vector format. Object projection in this simulation is calculated straightforwardly. If from each point source i, we obtain the cone beam projection P_i and the corresponding transmission $\exp(-P_i)$, then the object projection is calculated as

$$P_{object} = -\ln\left(\frac{\sum_i e^{-P_i}}{N}\right), \quad (1)$$

where N is the number of point sources. In this case, the normalization by N is the same as the flat field or open beam correction for the experimental data. Since projection is a non-dimensional quantity by its definition, the distance measure in the calculations is scaled to the non-dimensional pixel size of a discrete 3D model. Hence, the neutron attenuation coefficient μ has units of pixel^{-1}. Accordingly, the transition from a geometrical to a physical model is ensured by the relation:

$$pixel\ size\left[cm\right] = \mu\left[pixel^{-1}\right] / \mu\left[cm^{-1}\right] =$$
$$= \lambda\left[cm\right] / \lambda\left[pixel\right],$$

where λ is the mean free path of neutrons.

2. Radiography

Our calculation approach was tested by performing the modeling of classical edge-profile measurements with foil made of *Cd* or *Gd* (e.g., [8, 21]), which both have extremely high absorption of thermal neutrons as compared to other elements. If the foil is placed directly on the scintillator screen, then the observed unsharpness of the neutron image is related to the scintillator blurring. However, if the foil is placed at some distance l from the scintillator screen, the resulted blur will include the influence of the geometrical unsharpness U_g, controlled mainly by the L/D ratio, according to

$$U_g = \frac{D}{2}\left(\frac{l}{L-l} + \frac{l+w}{L-(l+w)}\right), \quad (2)$$

where w – thickness of the foil and l – distance between the foil face and the detector plane. We will not consider the influence of the scintillator on the resulting blur and focus only on the geometrical blurring. We considered a rectangular source with a width of 101 px, placed at distances of 2020 and 20200 px away from the detector. A highly absorbing foil with a total cross-section of 10^{10} pixel^{-1} and a thickness of 51 pixels was used. The foil phantom covers exactly half of the 513×513 image. Projections were acquired for different foil-to-detector distances in the range of 10 – 2000 px. U_g was calculated as a number of pixels having neither 0 nor 1 value across the boundary between foil and empty space (Fig. 2*a*). As expected, the blurring effect arising from the geometrical unsharpness becomes larger with increasing the foil-to-detector distance (Fig. 2*b*). Such an increase matches well with Eq. 2, which has almost linear relationship (Fig. 2*c*). The observed differences between U_g calculated from the modeling and those from Eq. 2 are only due to discretization effects.

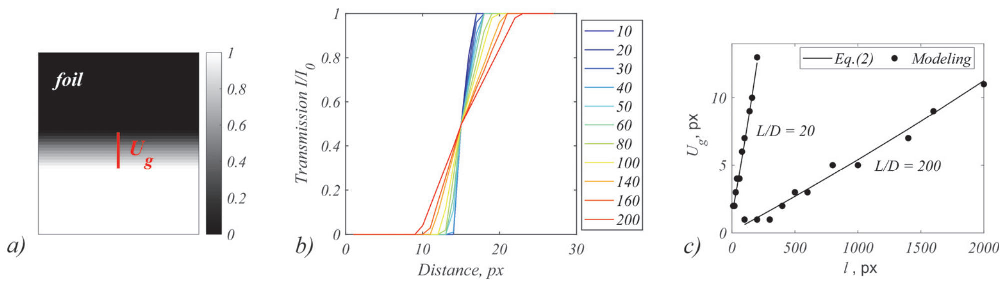

Fig. 2. Results of the simulation of the absorbing edge experiment: (a) transmission image; (b) cross-section across a boundary at different foil to detector distances (edge-spread function); (c) relationship in Eq. 2 calculated from the transmission images

The difference between divergent and parallel beams was further explored on a porous phantom. Phantom was obtained by placing pores with a random radius in a range of 1 – 20 px in a random position without overlaps within the 513×513×513 px volume. The attenuation coefficient of the skeleton was set to $0.005\ \mathrm{px}^{-1}$. The resulted volume was cropped to a cylinder with a radius of 254 px and a height of 493 px. In Fig. 3, the 3D porous phantom rendered with ImageJ [22].

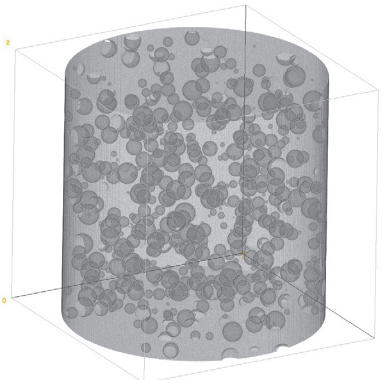

Fig. 3. Cylindrical porous phantom

We are interested in the simulation of neutron tomography and radiography, with the parameters being similar to those of a real station ones [23 – 24]: a pinhole-detector distance of up to 10 m, a disk-shaped source with a diameter of 2 cm, and a pixel size of 100 µm. For such a pixel size, $\mu = 0.5\ \mathrm{cm}^{-1}$ in our phantom. The calculated transmission images at zero rotation angle for the porous phantom (Fig. 3) placed at three distances $l = 1$ mm, 1 cm, and 5 cm from the detector plane are shown in Fig. 4 (upper row). The obtained images were compared with the parallel beam transmission by calculating the relative absolute difference (Fig. 4, bottom row)

RD = 100 %·|*divergent beam-parallel beam*| / (*parallel beam*).

The largest effect produced by the beam divergence occurs at the object's boundary, keeping the image center less influenced. From Fig. 4, it is also seen that the increase of L/D, as well as the decrease of l, favor low image degradation.

The quantity associated with an image degradation and combines L/D and l is the geometrical unsharpness of an infinitesimal material point:

$$u_g = \frac{lD}{L-l} = U_g\left(w=0\right) \approx \frac{l}{L/D}, \qquad (3)$$

where l – distance from the point to the detector. In the case of a 3D object, u_g can be evaluated for the object's center, and l in Eq. 3 becomes the sum of objects' face-to-detector distance and center-to-face distance.

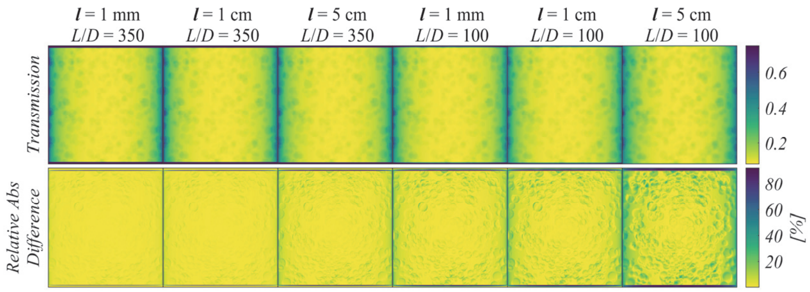

Fig. 4. Transmission images for different setup conditions (upper row) and their relative differences from the parallel beam transmission (lower row)

It is reasonable to expect the existence of the relation of u_g to *RD*, as both characterize the effect of a finite source. For sake of simplicity, we have not considered pixel-wise relations and calculated the mean value and standard deviation of *RD* for every case demonstrated in Fig. 4. The obtained results (Fig. 5) evidence the existence of a positive relationship between u_g and the characteristics of *RD*. The relations in Fig. 5 do not pretend to be general, as they may vary with the object composition and phase spatial distribution. However, we may roughly estimate the impact of the beam divergence on the transmission images. From Fig. 4, 5, it follows that the largest values of *RD* are mostly concentrated near the object boundaries, and the mean value does not exceed 10 % in the worst case. The signal-to-noise ratio (SNR) of a transmission image obtained in a radiography experiment is of the order of several dozens (e.g., [25]); therefore, image distortion may not depend as much on the beam divergence effect as on noise corruption, especially for low u_g. However, SNR depends on the exposure time and the parameters of the imaging system, including the type and thickness of the scintillator and the object's attenuation, which can significantly decrease the neutron count.

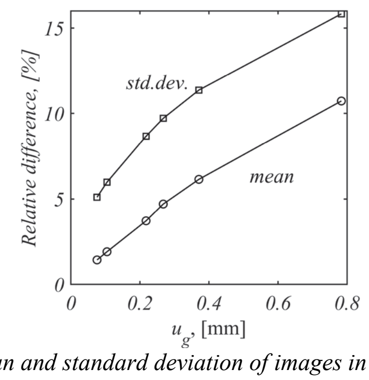

Fig. 5. Mean and standard deviation of images in a lower row of Fig. 4

3. Tomography

In the tomography experiment, either an object or a source with a detector has to be moved around. In our simulation, the source and detector move along a circle around an object's axis, which is equivalent to the rotation of an object around the same axis. Such movement is described by the same vectors used for defining the coordinates of the source and the detector [19].

In practice, during a single neutron tomography experiment regularly lasting about 4 hours, 361 transmission images with an angular step of 0.5° are acquired [23–24]. However, the simulation of such an experiment within the approach presented above would require an enormous amount of time: for the 2 cm disk-shaped source discretized by pixels of the same size as in the phantom, it would require 31417 times 361 cone beam projections. We reduced the number of point sources to 150 to achieve a reasonable computation time. Their spatial distribution approximates the disk shape in the same way as 31417 sources do (Fig. 6). Such replacement will introduce rather small errors into the simulated transmission images, as calculated for all six cases shown in Fig. 4: a maximum mean error of 0.03 % and an overall maximum error of 1.35 % met at the object's boundary.

The reconstruction of the 3D data from the simulated projections can be done by a variety of techniques, including filtered backprojection (FBP), simultaneous algebraic reconstruction technique (SART), simultaneous iterative reconstruction technique (SIRT), and conjugate gradient least squares (CGLS). We found that algebraic methods provide similar reconstruction results for our data, especially at high iteration numbers. Therefore, we set 1000 iterations of SIRT with a minimum value constrained to zero as a basic reconstruction algorithm in our work.

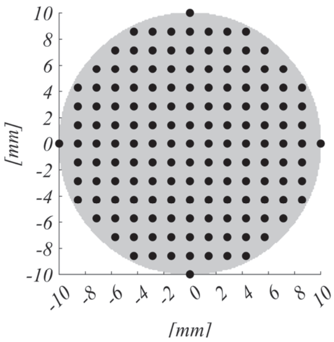

Fig. 6. Distribution of 150 point sources used in calculations

The reconstructed data was compared with the original binary 3D model and that obtained for an ideal case of parallel beam geometry. The most prominent effect of beam divergence that we observed was the shift of each pore from its real position in slices and in the 3D model. In Fig. 7, an example of such a shift is shown in a slice of one of the pores. Inspection of 2D slices made it clear, that the shift varies from slice to slice and from pore to pore. Tuning fork artifacts are present at pores boundaries (Fig. 7), as those appear due to the wrong center of rotation [26]. In this case, it is as if each pore would have its own center of rotation due to shift. As a result, the shape of the pores is also affected, making them more ovate. The geometrical unsharpness spanning into three dimensions causes artifacts of spurious objects in 2D slices (Fig. 7).

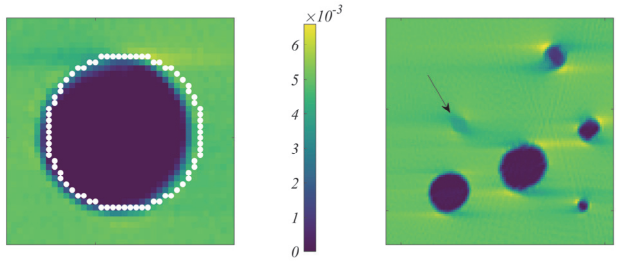

Fig. 7. Small patches selected from different places of the reconstructed slices with clearly visible artifacts. White circles denote the ground-truth boundary, and a black arrow points to the spurious object

Quantitatively, the shift can be evaluated from the binarized data as the distance between the centers of mass of the comparing pores. Individual thresholds (values of μ in pixel^{-1} or image brightness) were calculated for each pore by minimizing the difference between its volume and the volume of the corresponding ground truth pore. The calculated shifts are independent of the pore sizes, but they have a relation to the position of pores with respect to the object's center, as depicted in Fig. 8. It follows that the larger the distance from the object's center, the larger the shift will be. In addition, it is clearly seen that shifts increase along with the degree of unsharpness. In the case of $L/D = 200$ for a porous sample of ~ 5 cm in diameter the unsharpness may produce a maximum shift of 0.4 mm for a pore located near the object's boundary.

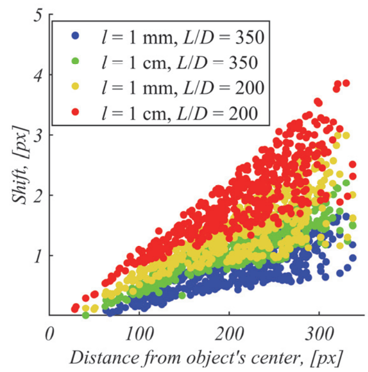

Fig. 8. The relationship between pores shifts with their distance from the object's center

Changes in pore shapes towards more ovate shapes were tracked using the sphericity parameter [27]. However, sphericity has shown much smaller deviations from the ground truth spherical shapes compared to shifts.

Geometrical unsharpness is not the single blurring agent in the experiment. Scintillator blur may have a larger contribution to image quality degradation. Its sample-independent PSF can be described numerically by a kernel for smoothing the transmission images (e.g., [28 – 29]). Gaussian filtering of transmission images with sigma of 0.5, 1.0, and 1.5 px was included in the present simulation as the scintillator blur, approximately corresponding to the blur of the LiF / ZnS:Ag scintillator of thickness in a range of 100 – 300 μm [8]. The result observed in the reconstructed data is similar to simple filtering: edges are blurred, tuning fork artifacts are smoothed, spurious objects remain or grow, and shifts are not canceled out. Regarding the problem of pore segmentation in neutron tomography data, it is important to identify the influence of both geometric unsharpness and scintillation blur on image binarization. First of all, it should be noted that individual thresholds do not depend on the position of the pore in space, unlike shifts. In cases where scintillation blur is not used, there is a dependence of the threshold on the pore diameter: the smaller the pore diameter, the higher the threshold will be (Fig. 9).

However, in the range $u_g = 0.8 - 1.8$ pixels (or 80 – 180 μm) used in this work, the thresholds change little and the average value is close to half the skeletal attenuation of 0.25 cm^{-1}. For a different value of skeletal attenuation, the average threshold will still be about half that. It follows that in a heterogeneous medium, the pore segmentation threshold depends on the attenuation distribution in the material surrounding the pore and can vary from pore to pore in proportion to its surroundings. The scintillator blur effect at σ = 0.5 and 1.0 pixels is comparable to geometric blur of 0.8 – 1.8 pixels. However, unlike the latter, the thresholds increase with increasing sigma of the Gaussian filter, and at σ = 1.5 pixels, the thresholds are determined only by the scintillator blur (Fig. 9). Therefore, in the case of a thick scintillator, the effect of beam divergence can be neglected, except for shift artifacts, as shown in Fig. 10. From Fig. 10, it also follows that the effect of beam divergence in NCT is spatially dependent due to shift and cannot be characterized by symmetric PSFs such as the Gaussian or Lorentzian kernels.

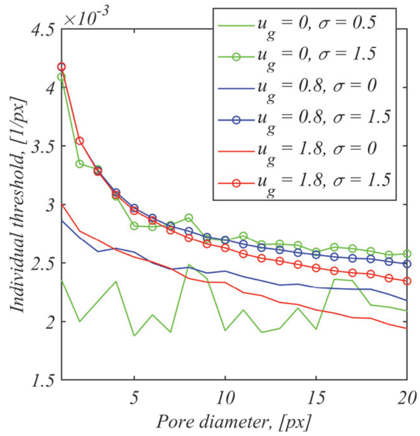

Fig. 9. The relationship of the mean pore threshold to the pore diameter in different cases of geometrical unsharpness and Gaussian blur

The quality of pores segmentation in neutron tomography data largely depends on the strength of all data corruption effects, such as sample-independent ones (reconstruction errors, beam divergence, scintillator blur) and due to sample (scattering background, beam hardening, signal-to-noise ratio). As outcomes from the present simulation, global segmentation techniques cannot provide optimal segmentation of pores due to spatially varied individual thresholds. This holds also for other corruption effects, such as secondary scattering background, which forms an effect of uneven illumination in the reconstructed data [30 – 31]. Therefore, the local segmentation methods proposed in [17, 32 – 33] for the segmentation of NCT and XCT data are advantageous as they deal with spatially dependent features.

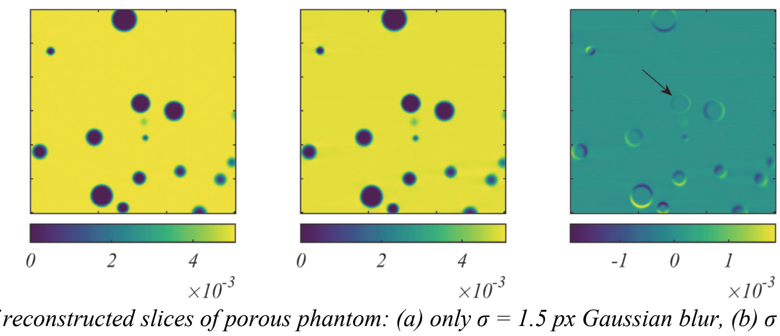

Fig. 10. Small patches of reconstructed slices of porous phantom: (a) only σ = 1.5 px Gaussian blur, (b) σ = 1.5 px Gaussian blur with u_g = 1.8 px (L/D = 200, l = 1cm) and their difference – (c). The black arrow points to the pore with the minimum shift among others in the slice

Conclusion

An approach to modeling beam divergence in neutron computed tomography using multiple point sources is presented. Its realization has been performed with a freeware ASTRA toolbox. As a result of modeling neutron computed tomography of a porous phantom, artifacts associated with the effect of beam divergence were identified, such as the shift of pores from their real positions in the phantom and tuning fork artifacts in slices. It is shown that the shifts depend on the position of the pores in the phantom and may reach several hundred microns for a sample of 5 cm in diameter and L/D ratios of at least up to 350. In addition, it is shown that the threshold for optimal binarization of a single pore in the reconstructed data is related to the pore size. The addition of scintillator blur can obscure the blur due to beam divergence while keeping shifts unaffected. However, the effect of beam divergence on the radiographic projections cannot be related to either Gaussian or Lorentzian point-spread functions.

References

[1] Podurets KM, Kichanov SE, Glazkov VP, Kovalenko ES, Murashev MM, Kozlenko DP, Lukin EV, Yatsishina EB. Modern methods of neutron radiography and tomography in studies of the internal structure of objects. Crystallogr Rep 2021; 66(2): 254-266. DOI: 10.1134/S1063774521020115.

[2] Zel IY, Petružálek M, Lokajíček T, Ivankina TI, Kichanov SE, Kozlenko DP, Porosnicu I, Schnabl P, Pruner P, Duliu OG. Assessment of structural, magnetic, and P-wave velocity anisotropy of two biotite gneisses from X-ray and neutron tomography. Tectonophysics 2021; 812: 228925. DOI: 10.1016/j.tecto.2021.228925.

[3] Kichanov SE, Kozlenko DP, Lukin EV, Rutkauskas AV, Krasavin EA, Rozanov AY, Savenko BN. A neutron tomography study of the Seymchan pallasite. Meteorit Planet Sci 2018; 53(10): 2155-2164. DOI:10.1111/maps.13115.

[4] Lehmann E, Mannes D, Kaestner A, Grünzweig C. Recent applications of neutron imaging methods. Phys Procedia 2017; 88: 5-12. DOI: 10.1016/j.phpro.2017.06.055.

[5] Vontobel P, Lehmann EH, Hassanein R, Frei G. Neutron tomography: Method and applications. Phys B: Condens Matter 2006; 385-386: 475-480. DOI: 10.1016/j.physb.2006.05.252.

[6] Schillinger B, Lehmann E, Vontobel P. 3D neutron computed tomography: requirements and applications. Phys B: Condens Matter 2000; 276-278: 59-62. DOI: 10.1016/s0921-4526(99)01254-5.

[7] Masschaele B, Dierick M, Van Hoorebeke L, Jacobs P, Vlassenbroeck J, Cnudde V. Neutron CT enhancement by iterative de-blurring of neutron transmission images. Nucl Instrum Methods Phys Res Section A: Accel Spectrom Detect Assoc Equip 2005; 542(1-3): 361-366. DOI: 10.1016/j.nima.2005.01.162.

[8] Baechler S, Kardjilov N, Dierick M, Jolie J, Kühne G, Lehmann E, Materna T. New features in cold neutron radiography and tomography: Part I: thinner scintillators and a neutron velocity selector to improve the spatial resolution. Nucl Instrum Methods Phys Res Section A: Accel Spectrom Detect Assoc Equip 2002: 491(3): 481-491. DOI: 10.1016/s0168-9002(02)01238-x.

[9] Williams SH, Hilger A, Kardjilov N, Manke I, Strobl M, Douissard PA, Martin T, Riesemeier H, Banhart J. Detection system for microimaging with neutrons. J Instrum 2012; 7(2): P02014. DOI: 10.1088/1748-0221/7/02/P02014.

[10] Smith SW. The scientist and engineer's guide to digital Signal processing. San Diego: California Technical Publishing; 1999. ISBN: 978-0966017632.

[11] Datta A, Hawari AI. Performance evaluation in transmission neutron tomography using Geant4. Proc IEEE Nuclear Science Symposium and Medical Imaging Conf (NSS/MIC) 2017: 1-6. DOI: 10.1109/NSSMIC.2017.8532680.

[12] Hassanein R, Lehmann E, Vontobel P. Methods of scattering corrections for quantitative neutron radiography. Nucl Instrum Methods Phys Res Section A: Accel Spectrom Detect Assoc Equip 2005; 542(1-3): 353-360. DOI: 10.1016/j.nima.2005.01.161.

[13] Hassanein R, de Beer F, Kardjilov N, Lehmann E. Scattering correction algorithm for neutron radiography and tomography tested at facilities with different beam characteristics. Phys B: Condens Matter 2006; 385-386: 1194-1196. DOI: 10.1016/j.physb.2006.05.406.

[14] Kaestner AP, Trtik P, Zarebanadkouki M, Kazantsev D, Snehota M, Dobson KJ, Lehmann EH. Recent developments in neutron imaging with applications for porous media research. Solid Earth 2016; 7(5): 1281-1292. DOI: 10.5194/se-7-1281-2016.

[15] Zhang P, Wittmann FH, Lura P, Müller HS, Han S, Zhao T. Application of neutron imaging to investigate fundamental aspects of durability of cement-based materials: A review. Cem Concr Res 2018; 108: 152-166. DOI: 10.1016/j.cemconres.2018.03.003.

[16] Kichanov SE, Nazarov KM, Kozlenko DP, Balasoiu M, Nicu M, Ionascu L, Dragolici AC, Dragolici F, Savenko BN. Neutron tomography studies of cement-based materials used for radioactive waste conditioning. Rom J Phys 2019; 62(803): 9.

[17] Zel I, Kenessarin M, Kichanov S, Nazarov K, Bălășoiu M, Kozlenko D. Pore segmentation techniques for low-resolution data: Application to the neutron tomography data of cement materials. J Imaging 2022; 8(9): 242. DOI: 10.3390/jimaging8090242.

[18] Van Aarle W, Palenstijn WJ, De Beenhouwer J, Altantzis T, Bals S, Batenburg KJ, Sijbers J. The ASTRA Toolbox: A platform for advanced algorithm development in electron tomography. Ultramicroscopy 2015; 157: 35-47. DOI: 10.1016/j.ultramic.2015.05.002.

[19] Van Aarle W, Palenstijn WJ, Cant J, Janssens E, Bleichrodt F, Dabravolski A, de Beenhouwer J, K. Batenburg J, Sijbers J. Fast and flexible X-ray tomography using the ASTRA toolbox. Opt Express 2016; 24(22): 25129-25147. DOI: 10.1364/oe.24.025129.

[20] Palenstijn WJ, Bédorf J, Sijbers J, Batenburg KJ. A distributed ASTRA toolbox. Adv Struct Chem Imaging 2016; 2: 19. DOI: 10.1186/s40679-016-0032-z.

[21] Lange C, Bernt N. Neutron imaging at the low flux training and research reactor AKR-2. Nucl Instrum Methods Phys Res Section A: Accel Spectrom Detect Assoc Equip 2019; 941: 162292. DOI: 10.1016/j.nima.2019.06.033.

[22] Schneider CA, Rasband WS, Eliceiri KW. NIH Image to ImageJ: 25 years of image analysis. Nat Methods 2012; 9(7): 671-675. DOI: 10.1038/nmeth.2089.

[23] Kozlenko DP, Kichanov SE, Lukin EV, Rutkauskas AV, Belushkin AV, Bokuchava GD, Savenko BN. Neutron radiography and tomography facility at IBR-2 reactor. Phys Part Nucl Lett 2016; 13(3): 346-351. DOI: 10.1134/s1547477116030146.

[24] Nazarov KM, Muhametuly B, Kenzhin EA, Kichanov SE, Kozlenko DP, Lukin EV, Shaimerdenov AA. New neutron radiography and tomography facility TITAN at the WWR-K reactor. Nucl Instrum Methods Phys Res Section A: Accel Spectrom Detect Assoc Equip 2020; 982: 164572. DOI: 10.1016/j.nima.2020.164572.

[25] Grünauer F. Design, optimization, and implementation of the new neutron radiography facility at FRM-II. The thesis for the doctor of natural sciences. München; 2005.

[26] Shepp LA, Hilal SK, Schulz RA. The tuning fork artifact in computerized tomography. Comput Graph Image

Process 1979; 10(3): 246-255. DOI: 10.1016/0146-664x(79)90004-2.
[27] Wadell H. Volume, shape, and roundness of rock particles. J Geol 1932, 40(5): 443-451. DOI: 10.1086/623964.
[28] Cha BK, Lee Y, Kim K. Development of adaptive point-spread function estimation method in various scintillation detector thickness for X-ray imaging. Sensors 2023; 23(19): 8185. DOI: 10.3390/s23198185.
[29] Saito Y, Ito D. 3D velocity vector measurements in a liquid-metal using unsharpness in neutron transmission images. Mater Res Proc 2020; 15: 281-286. DOI: 10.21741/9781644900574-44.
[30] Boillat P, Carminati C, Schmid F, Grünzweig C, Hovind J, Kaestner A, Mannes D, Morgano M, Siegwart M, Trtik P, Vontobel P, Lehmann EH. Chasing quantitative biases in neutron imaging with scintillator-camera detectors: a practical method with black body grids. Opt Express 2018; 26(12): 15769-15784. DOI: 10.1364/OE.26.015769.
[31] Raventos M, Harti RP, Lehmann E, Grünzweig C. A method for neutron scattering quantification and correction applied to neutron imaging. Phys Procedia 2017; 88: 275-281. DOI: 10.1016/j.phpro.2017.06.038.
[32] Wonho Oh, Lindquist B. Image thresholding by indicator kriging. IEEE Trans Pattern Anal Mach Intell 1999; 21(7): 590-602. DOI: 10.1109/34.777370.
[33] Hapca SM, Houston AN, Otten W, Baveye PC. New local thresholding method for soil images by minimizing grayscale intra-class variance. Vadose Zone J 2013; 12(3): 1-13. DOI: 10.2136/vzj2012.0172.

Author's information

Ivan Yurievich Zel, (b.1990), studied at Tula State University. Received his Ph.D. degree in Condensed Matter Physics (2017). Works as a researcher at the Frank Laboratory of Neutron Physics of the Joint Institute for Nuclear Research. Research interests: neutron tomography, image processing, neutron and X-ray diffraction at high pressures, seismic anisotropy. E-mail: *zel@jinr.ru*

Received December 14, 2023. The final version – June 11, 2024.